Supporting Information

Barton and Brewer 10.1073/pnas.1423673112

SI Materials and Methods

Anatomical Data. Scanning was conducted at the University of California, Irvine, on the 3T Philips Achieva MR Scanner with an eight-channel sensitivity encoding (SENSE) imaging head coil. One high-resolution whole-brain anatomical dataset was acquired for each subject [T1-weighted 3D magnetization-prepared rapid acquisition with gradient echo (MPRAGE), 1-mm^3 voxels, repetition time (TR) = 8.4 ms, echo time (TE) = 3.7 ms, flip = 8°, SENSE factor = 2.4]. We used custom software (mrVista from Stanford University; white.stanford.edu/software) (1) to segment white matter, which was hand-edited to minimize segmentation errors. Gray matter was grown from the segmented white matter to form a 2- to 4-mm layer covering the white matter surface. The cortical surface was then represented as a mesh at the white-/gray-matter border, which was used to render a smooth 3D cortical surface and flatten the cortical representation for visualization of the visual field maps (2).

In addition, one anatomical in-plane image was acquired before each set of functional scans with the same slice prescription as the functional scans but a slightly higher spatial resolution (1 × 1 × 3-mm voxels). These anatomical image slices were physically in register with the functional image slices to align the functional data with the high-resolution anatomical data. This alignment was performed by first, a manual coregistration and then, a semiautomated 3D coregistration algorithm, which used a mutual information method (3, 4).

Functional Data. The same 3T scanner was used to collect the functional MR data, with ∼35 axial slices oriented approximately parallel to the calcarine sulcus (T2-weighted, gradient echo imaging, TR = 2 s, TE = 30 ms, flip = 90°, SENSE factor = 1.7, reconstructed voxel size of 1.875 × 1.875 × 3 mm, no gap). We analyzed fMRI data using the same custom Matlab mrVISTA software. For each subject, data in each fMRI session were analyzed voxel by voxel with no spatial smoothing. The mean value maps of the blood oxygen level-dependent (BOLD) signals were examined for potential head movements. No motion correction algorithm was applied here, because all scans had less than one voxel of head motion. The time series from each scan was high-pass filtered to remove low-frequency sources of physiological noise and averaged together to form one mean time series for each subject, which was then used in the pRF model analysis (5).

Stimulus Presentation. Stimuli were generated using the Psychophysics Toolbox (6) in the Matlab programming environment on a Dell Optiplex desktop. Stimuli were back-projected onto a screen at the head end of the bore of the magnet by a Christie DLV1400-DX DLP Projector (spatial resolution: 1,024 × 768 pixels, refresh rate: 60 Hz). Subjects viewed the display on an angled front surface mirror mounted on the head coil close to the eyes with a viewing distance of ∼70 cm. Head movements were minimized with padding and tape. Photopic conditions (maximum luminance = 140 cd/m^2) consisted of our standard setup for visual field mapping experiments, with lights of the scanning room turned on and a neutral density filter over the projector's wave guide. Scotopic conditions (maximum luminance = 0.003 cd/m^2) during scanning were created by blacking out all light sources in the scanner room and placing additional neutral density filters over the projector's wave guide. Subjects were dark-adapted for 35–40 min before any set of scotopic scans and light-adapted for at least 10 min before any set of photopic scans (7, 8). We also verified dark adaptation at the start of each scotopic scan session by testing each subject's inability to perceive stimuli within the central 2° radius from fixation (i.e., within the rod scotoma).

Visual Field Mapping Stimuli. The moving bar stimulus was comprised of achromatic (mean luminance ∼50 cd/m^2) dynamic checkerboard contrast patterns (∼90% contrast) and spanned a visual field subtending a maximum radius of 11° of visual angle (Fig. 2*F*). The contrast pattern of the bar aperture consisted of rows that appeared to be moving in the opposite direction to adjacent rows, with each column spanning the length of the bar aperture and each row spanning its width. The bar apertures were displaced in discrete steps every 2 s in synchrony with the fMRI volume acquisition. Modulation of the checkerboard contrast pattern was metameric to modulation of a 500-nm light. The contrast pattern motion created a 2-Hz temporal frequency, and the motion direction changed randomly every 2–3 s. Four bar orientations (0°, 45°, 90°, and 135° from vertical) with two motion directions orthogonal to each orientation were used. This stimulus set produced eight different bar configurations and a total presentation time of 192 s at one cycle per scan. Four mean luminance periods were inserted in the last 12 s of each 48-s period at a frequency of four cycles per scan. To aid fixation under scotopic conditions, subjects maintained fixation on one of two large central crosses, which alternated between spanning either the diagonals from the corners of the field of view or the midpoints of each of the sides of the field of view. The same two alternating fixation crosses were used in both scotopic and photopic luminance conditions. The lines of each fixation cross were roughly 0.5° wide, and they randomly switched between the two positions every 2–4 s as a drifting bar moved passed across the visual field. Subjects attended to these moving bar apertures and responded with a button press to an intermittent, subtle change in the motion direction of the checkerboard pattern (not in sync with the visual stimulus position changes or mean luminance periods).

Assessment of Fixation Stability. Subjects were required to fixate their eyes under photopic conditions, where the fixation cross is clearly visible at the center of vision, and scotopic conditions, where the center of the fixation cross overlaps the rod scotoma. As a result, we checked the possibility that differences in fixation stability may have affected our results. Previous work modeling the effects of eye movements shows that eye movements would have relatively uniform effects across the entire visual field and that the measurements of visual field maps using pRF modeling remain relatively unaffected by artificial or central scotomas that could produce a small to moderate range of eye movements (9–12). Each of our effects is only over a portion of the visual field (either central or peripheral eccentricities). As a precaution, our fixation stimuli were specifically designed to minimize differences in eye movements and fixation difficulty between conditions by being large and extending to the borders of the field of view (13). Additionally, the fixation cross changed from a large X shape to a large + shape at jittered intervals to diminish consistent effects of fixation stability and additional aid fixation. Our subjects also underwent extensive training and practice with our stimuli under both photopic and scotopic conditions as well as other many other studies that require fixation. Subjects who are experts at fixating, such as our subjects were, perform better than nonexperts at fixation tasks (9, 14).

Eye tracking was provided by an MRI-compatible long-range remote tracking system (Applied Science Laboratories). Any

scans with excessive eye movements were discarded from additional analysis (<1% of all scans). To confirm that eye movements did not differ between photopic and scotopic conditions, additional analyses were performed. The degree to which eye movements occurred during a scan can be measured as the variability of BOLD modulation in the eyes (Eyes ROI) (9). If the SD of the BOLD signal in the Eyes ROI across subjects between photopic and scotopic conditions was significantly different, it would indicate that there were differences in eye movements (Fig. S4 and Table S1). However, a paired samples t test reveals no difference between photopic and scotopic conditions [t (2) = −0.318, P = 0.781], indicating that eye movements did not significantly vary between conditions and thus, did not significantly contribute to our results. For comparison, scotopic eye movements were compared with an eye saccade task, where subjects were asked to make a series of saccadic eye movements from fixation to positions in the midperiphery of the presently measured visual field. As expected, a paired samples t test revealed a significant difference between scotopic and eye saccade scans [t (2) = −5.070, P = 0.037], indicating that eye movements were not a significant factor in scotopic scans.

To rule out the possibility that the difference between scotopic and eye saccade scans in the Eyes ROI was caused by some other factor unrelated to eye movements, we compared the SD of BOLD modulation in V1 between the conditions (Fig. S4 and Table S1). As expected, a paired samples t test reveals no difference between scotopic and eye saccade scans [t (2) = −2.339, P = 0.144], indicating that the difference observed between the scans in the Eyes ROI is related to the difference in eye movements between the conditions. Similarly, there was no difference between photopic and scotopic scans in the SD of BOLD modulation in V1, which was revealed by a paired samples t test [t (2) = 0.574, P = 0.624].

In sum, although it was unlikely that differences in fixation may have influenced our results, these measurements confirm that there was no significant difference in eye movements between luminance conditions.

pRF Modeling Analysis. We used the pRF modeling method to estimate the V1, V2, V3, hV4, and VO-1 visual field maps and pRFs. The pRF for a particular voxel is defined as the region of visual space that preferentially activates that cortical site (complete details are in ref. 5). In each voxel, the BOLD response to our stimuli was predicted using a 2D Gaussian pRF model with parameters of preferred center location (x, y) and size (spread; σ). The predicted fMRI time series was calculated by convolving the model pRF with the stimulus sequence and BOLD hemodynamic response function (15, 16). The pRF parameters for each voxel minimized the sum of squared errors between the predicted and observed fMRI time series for the bar apertures.

Each voxel was independently evaluated in terms of the variance of the time series explained by the best-fitting model. In the typical traveling wave measurement of visual field maps, each voxel is independently assigned a coherence value, which is equal to the amplitude of the BOLD signal modulation at the stimulus frequency divided by the square root of the power of the BOLD modulation at all other frequencies except the first and second harmonics. pRF modeling uses percentage variance explained as a primary measurement of goodness of fit; here, we convert to coherence values for comparison with typical phase-encoded traveling wave visual field mapping studies (5, 17–19). Only voxels with coherence values exceeding 0.20 corresponding to that voxel's peak response to the stimuli presented were considered for additional analysis (20, 21). We have measured the noise in visual cortex using baseline measurements in early visual cortex with a combination of approaches, including photopic and scotopic visual stimuli (bars, wedges, and rings) with traveling wave and pRF modeling methods. Our measurements show maximum baseline noise levels for coherence (from traveling wave measurements) of 0.15 and variance explained (from pRF modeling measurements) of 0.03.

Eccentricity [$\sqrt{(x^2+y^2)}$] and angle [$\tan^{-1}(y/x)$] were derived from the 2D Gaussian models and are plotted on the unfolded cortical surface measured in each subject (Fig. 2 and Fig. S2). The pRF model prediction assumed full stimulation of the visual field out to 11° radius; the model was not constrained by the expected presence of the rod scotoma (11). The sizes of pRFs (σ in degrees of visual angle) are presented as a function of eccentricity collapsed across subjects (Fig. S7).

Definition of Visual Field Maps. We define a visual field map as a complete map by the following criteria: (*i*) it represents a complete contralateral hemifield of visual space (visual field maps vary in the degree to which their pRFs extend into ipsilateral space, and therefore, we ignore the extent of ipsilateral representation in this definition; also, we group the discontiguous V2 and V3 dorsal/ventral quarterfields into complete hemifield representations), (*ii*) both a polar angle and an eccentricity representation must be present, and (*iii*) the polar angle and eccentricity representations are orthogonal to one another (22). When presented with reversals in polar angle or eccentricity representations, which denote the borders between visual field maps, we split the reversal evenly between the two maps. Here, we follow widely established conventions for the definitions of the posterior and ventral occipital visual field maps V1, V2, V3, hV4, and VO-1 (Fig. 2 and Fig. S2) (19, 21, 23–25).

1. Teo PC, Sapiro G, Wandell BA (1997) Creating connected representations of cortical gray matter for functional MRI visualization. *IEEE Trans Med Imaging* 16(6):852–863.
2. Wandell BA, Chial S, Backus BT (2000) Visualization and measurement of the cortical surface. *J Cogn Neurosci* 12(5):739–752.
3. Maes F, Collignon A, Vandermeulen D, Marchal G, Suetens P (1997) Multimodality image registration by maximization of mutual information. *IEEE Trans Med Imaging* 16(2):187–198.
4. Nestares O, Heeger DJ (2000) Robust multiresolution alignment of MRI brain volumes. *Magn Reson Med* 43(5):705–715.
5. Dumoulin SO, Wandell BA (2008) Population receptive field estimates in human visual cortex. *Neuroimage* 39(2):647–660.
6. Pelli DG (1997) The VideoToolbox software for visual psychophysics: Transforming numbers into movies. *Spat Vis* 10(4):437–442.
7. Barlow HB, Sparrock JM (1964) The role of afterimages in dark adaptation. *Science* 144(3624):1309–1314.
8. Hecht S, Haig C, Wald G (1935) The dark adaptation of retinal fields of different size and location. *J Gen Physiol* 19(2):321–337.
9. Beauchamp MS (2003) Detection of eye movements from fMRI data. *Magn Reson Med* 49(2):376–380.
10. Kimmig H, et al. (2001) Relationship between saccadic eye movements and cortical activity as measured by fMRI: Quantitative and qualitative aspects. *Exp Brain Res* 141(2):184–194.
11. Haak KV, Cornelissen FW, Morland AB (2012) Population receptive field dynamics in human visual cortex. *PLoS ONE* 7(5):e37686.
12. Levin N, Dumoulin SO, Winawer J, Dougherty RF, Wandell BA (2010) Cortical maps and white matter tracts following long period of visual deprivation and retinal image restoration. *Neuron* 65(1):21–31.
13. Thaler L, Schütz AC, Goodale MA, Gegenfurtner KR (2013) What is the best fixation target? The effect of target shape on stability of fixational eye movements. *Vision Res* 76:31–42.
14. Guzman-Martinez E, Leung P, Franconeri S, Grabowecky M, Suzuki S (2009) Rapid eye-fixation training without eyetracking. *Psychon Bull Rev* 16(3):491–496.
15. Boynton GM, Engel SA, Glover GH, Heeger DJ (1996) Linear systems analysis of functional magnetic resonance imaging in human V1. *J Neurosci* 16(13):4207–4221.
16. Friston KJ, et al. (1998) Event-related fMRI: Characterizing differential responses. *Neuroimage* 7(1):30–40.
17. Amano K, Wandell BA, Dumoulin SO (2009) Visual field maps, population receptive field sizes, and visual field coverage in the human MT+ complex. *J Neurophysiol* 102(5):2704–2718.
18. Brewer AA, Barton B (2014) Visual cortex in aging and Alzheimer's disease: Changes in visual field maps and population receptive fields. *Front Psychol* 5:74.
19. Wandell BA, Dumoulin SO, Brewer AA (2007) Visual field maps in human cortex. *Neuron* 56(2):366–383.
20. Baseler HA, et al. (2002) Reorganization of human cortical maps caused by inherited photoreceptor abnormalities. *Nat Neurosci* 5(4):364–370.
21. Brewer AA, Liu J, Wade AR, Wandell BA (2005) Visual field maps and stimulus selectivity in human ventral occipital cortex. *Nat Neurosci* 8(8):1102–1109.

22. Brewer AA, Barton B (2012) Visual field map organization in human visual cortex. *Visual Cortex—Current Status and Perspectives*, eds Molotchnikoff S, Rouat J (InTech, New York), pp 29–60.
23. Dougherty RF, et al. (2003) Visual field representations and locations of visual areas V1/2/3 in human visual cortex. *J Vis* 3(10):586–598.
24. Wandell BA, Brewer AA, Dougherty RF (2005) Visual field map clusters in human cortex. *Philos Trans R Soc Lond B Biol Sci* 360(1456):693–707.
25. Wandell BA, Winawer J (2011) Imaging retinotopic maps in the human brain. *Vision Res* 51(7):718–737.

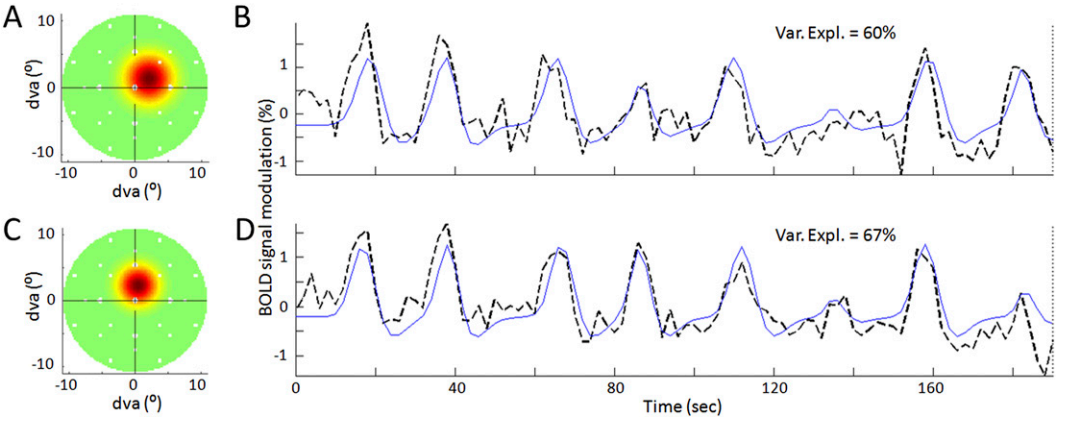

Fig. S1. pRF model fits for a single typical V1 voxel at the rod scotoma edge. The measurements for *A* and *B* were taken under photopic conditions from the same voxel at the edge of the rod scotoma in V1 of subject 3, whereas *C* and *D* were under scotopic conditions. *A* and *C* show representations of visual space and the portion of it represented by the population of neurons in this V1 voxel (the result of the pRF model fit). Red/yellow colors depict the regions of visual space represented by the example voxel. Green color represents no response. *B* and *D* show the percentage of BOLD modulation over time. The black dotted lines represent actual data; the solid blue lines represent the pRF model fit. The variance explained (Var. Expl.) by each model fit is displayed above each graph. Note the correspondence between the pRF model fit and the data in each case. dva, Degrees of visual angle.

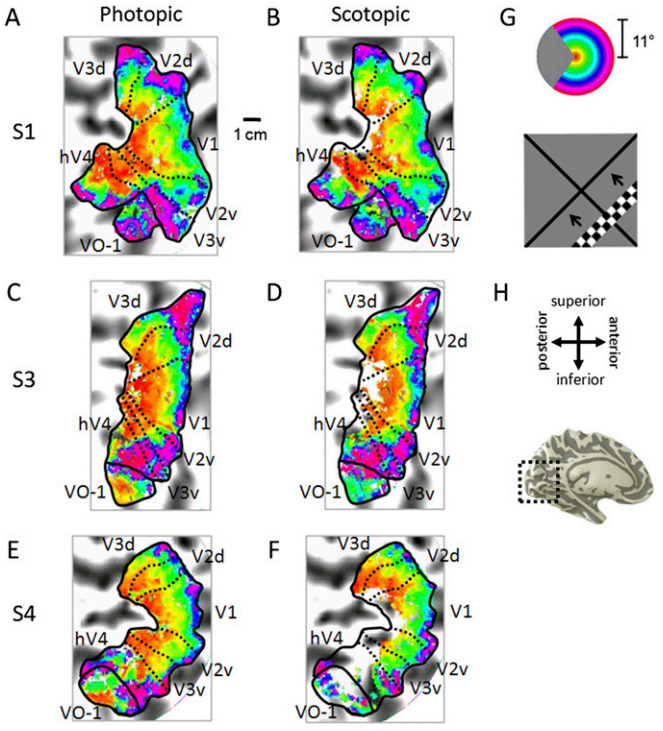

Fig. S2. Eccentricity maps in photopic and scotopic conditions. (*A*–*F*) Pseudocolor overlays on a flattened representation of occipital cortexes from three subjects represent the eccentricity position in visual space that produces the strongest response at that cortical location. Data for subject S2 are presented in Fig. 2. (*A*, *C*, and *E*) Photopic measurements. (*B*, *D*, and *F*) Scotopic measurements. Boundaries of visual field maps are depicted with dotted (boundaries along polar angle reversals) and solid (boundaries along eccentricity reversals and the edge of measurement) black lines. Coherence ≥ 0.20. (Scale bar: 1 cm along the flattened cortical surface.) (*G*, *Upper*) Color legend represents the visual field from 0° to 11° radius. (*G*, *Lower*) Moving bar stimulus for visual field map and pRF measurements comprised a set of contrast-reversing checkerboard patterns at eccentricities from 0° to 11° radius. One frame is shown for the bar stimulus sequence. Four bar orientations (0°, 45°, 90°, and 135° from vertical) with two motion directions orthogonal to each orientation were used, producing eight different bar configurations. (*H*, *Upper*) Anatomical orientation legend. (*H*, *Lower*) Inflated 3D representation of a medial view of a representative left hemisphere from which all data were taken. The black dotted line indicates the region near the calcarine sulcus of the occipital lobe, where the maps were measured.

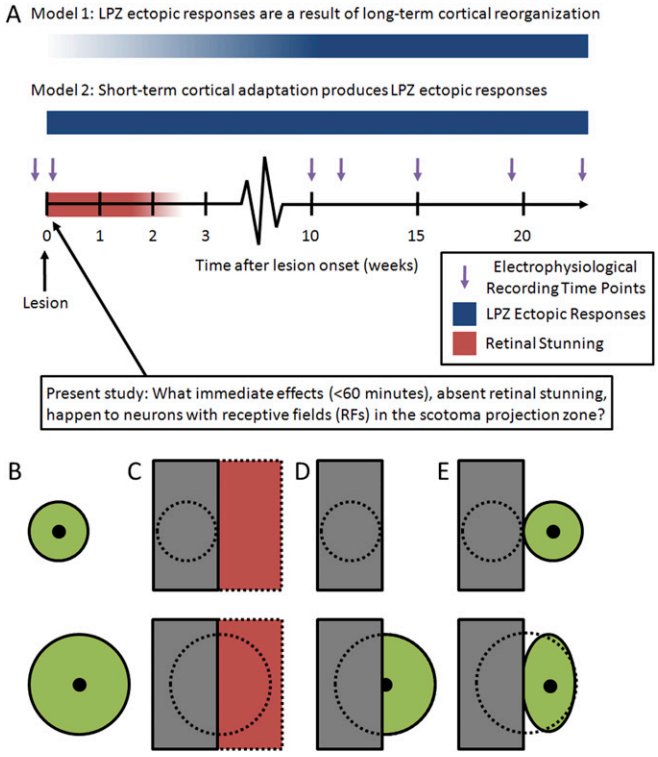

Fig. S3. Models to explain ectopic responses in scotoma projection zones (SPZs). (*A*) Model 1 assumes that ectopic responses of neurons with RFs in the SPZ are not an aspect of the normal RF organization of the visual system but happen only after extensive cortical reorganization. Model 2 assumes that ectopic responses of neurons with RFs in the SPZ are the expected response of the normal RF organization of the visual system. The key time point to differentiate between these two models is immediately after the onset of a scotoma, which for all scotomas induced by damage, is contaminated by stunning of cells in and around the lesion site. The rod scotoma is a naturally occurring, reversible scotoma that that can be applied noninvasively to a primate without inducing damage and rendering immediate measurements of RFs interacting with the SPZ uninterpretable. (*B–E*) Potential confounds in measurements of long-term reorganization and short-term adaptation. *Upper* represents the RF of a cortical neuron or the pRF of a single voxel, which is completely eclipsed by a retinal scotoma. *Lower* represents the RF of a cortical neuron or the pRF of a single voxel, which is partially eclipsed by a retinal scotoma. In each panel, solid lines indicate an active cortical (p)RF, and dotted lines indicate a silenced, original cortical (p)RF. *B* represents the original cortical (p)RFs, with dots as the preferred centers and circles as the spreads. (*C*) Here, both (p)RFs are silenced because of a combination of the retinal scotoma and the adjacent retinal stunning, which occurs in studies involving the creation of a direct lesion to the retinae (1–3). This combination of scotoma and retinal stunning effectively broadens the silenced cortical region. *D* represents the new effective cortical (p)RFs after recovery from retinal stunning (~2 wk in retinal lesion studies using photocoagulation) but before extensive long-term reorganization. Note that (*Upper*) the totally eclipsed cortical (p)RF remains silenced, whereas (*Lower*) the partially eclipsed (p)RF is active for the portion of the p(RF) that was silenced by retinal stunning. Such recovery from retinal stunning is impossible to differentiate at this point from long-term cortical reorganization. In addition, *D* also depicts the immediate measurements of scotomas, such as the rod scotoma presented here or artificial scotomas (4), which do not involve retinal stunning. This type of short-term (p)RF change must be accounted for in studies of long-term reorganization. *E* represents examples of potential long-term reorganization for these cortical (p)RFs. In *Upper*, the cortical (p)RF that was initially fully covered by the scotoma has now shifted to represent new regions of visual space. However, in *Lower*, this same shift into new territory cannot be distinguished by these (p)RF measurements from the measurements of the expected leftover (p)RF seen in *D*, *Lower*.

1. Smirnakis SM, et al. (2005) Lack of long-term cortical reorganization after macaque retinal lesions. *Nature* 435(7040):300–307.
2. Giannikopoulos DV, Eysel UT (2006) Dynamics and specificity of cortical map reorganization after retinal lesions. *Proc Natl Acad Sci USA* 103(28):10805–10810.
3. Wandell BA, Smirnakis SM (2009) Plasticity and stability of visual field maps in adult primary visual cortex. *Nat Rev Neurosci* 10(12):873–884.
4. Haak KV, Cornelissen FW, Morland AB (2012) Population receptive field dynamics in human visual cortex. *PLoS ONE* 7(5):e37686.

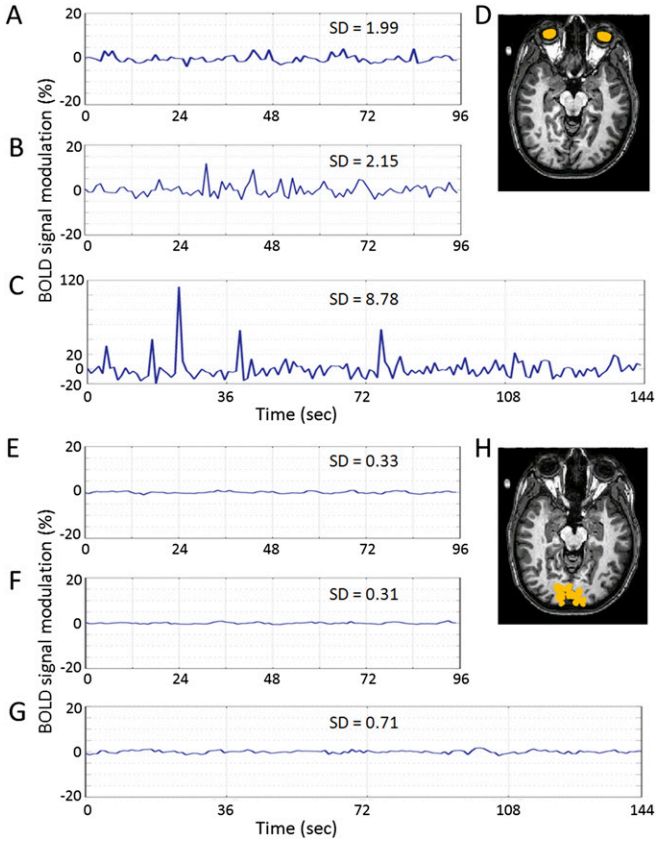

Fig. S4. Eye movement measurements. Each graph represents the BOLD signal modulation in percentage over time for one scan for an individual subject. Measurements for *A*–*C* are taken from (*D*) the Eyes ROI. In general, the more that the subjects moved their eyes, the higher the variations in BOLD as measured by the SDs for measurements from the Eyes ROI. A paired samples *t* test reveals that there is not a significant difference in the SD between (*A*) photopic and (*B*) scotopic conditions [t (2) = −0.318, P = 0.781], indicating no difference in eye movements (Table S2). For comparison, *C* represents the BOLD variation in a task where subjects were required to make a series of eye saccades, which has significantly higher SD than in *B* [t (2) = −5.070, P = 0.037]. Note that a different scale is used for *C* than the other graphs; 20% BOLD modulation is indicated for scale comparison. Measurements for *E*–*G* are taken from (*H*) bilateral V1, which should not vary between conditions, even if eye movements did. A paired samples *t* test reveals no difference between (*E*) photopic and (*F*) scotopic conditions in the V1 ROI [t (2) = 0.574, P = 0.624] or (*G*) scotopic and eye saccade conditions [t (2) = −2.339, P = 0.144] (Table S2), ruling out task differences unrelated to eye movements between the eye saccade and scotopic conditions in (*A*–*D*) the Eyes ROI comparisons.

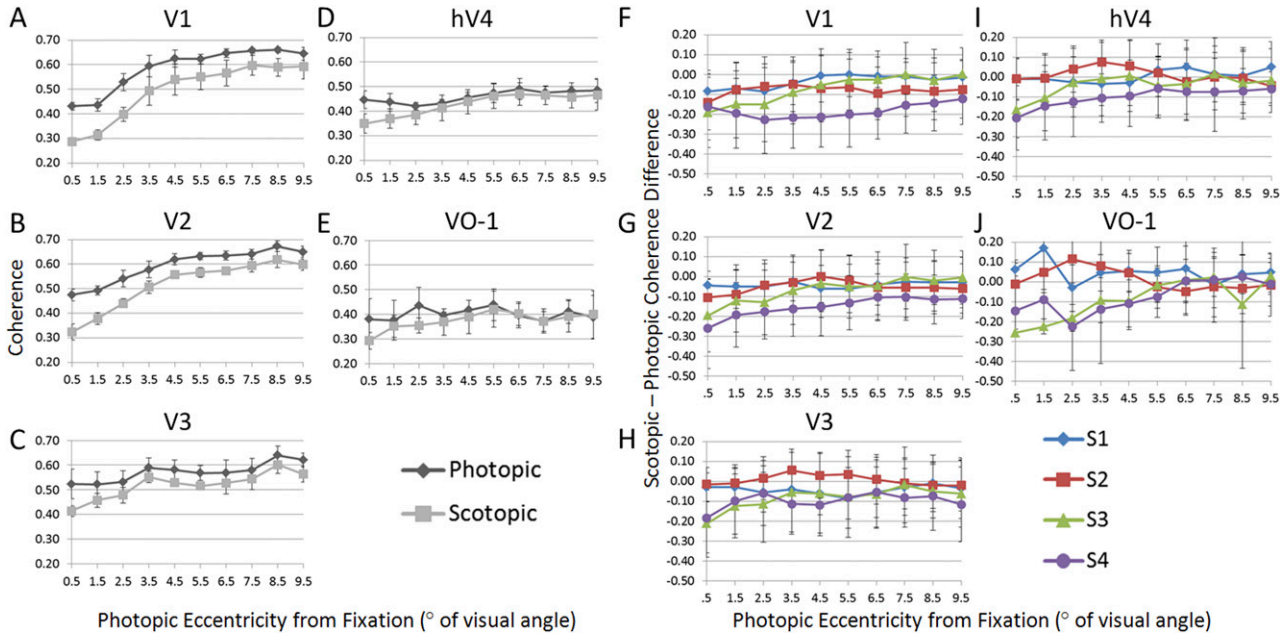

Fig. S5. Coherence under photopic and scotopic conditions. (*A*–*E*) Each graph displays coherence for photopic (dark gray lines with diamonds) and scotopic (light gray lines with squares) conditions in a single visual field map as a function of preferred eccentricity under photopic conditions averaged across subjects. (*A*) V1 coherence. (*B*) V2 coherence. (*C*) V3 coherence. (*D*) hV4 coherence. (*E*) VO-1 coherence. Note the relatively greater drop in coherence for scotopic relative to photopic conditions in the central eccentricities of each map. Error bars represent SEMs. (*F*–*J*) Each graph displays the coherence difference (scotopic – photopic) for each map for each individual subject. (*F*) V1 coherence difference. (*G*) V2 coherence difference. (*H*) V3 coherence difference. (*I*) hV4 coherence difference. (*J*) VO-1 coherence difference. The legend indicates the color and marker shape for each subject. Error bars represent SDs.

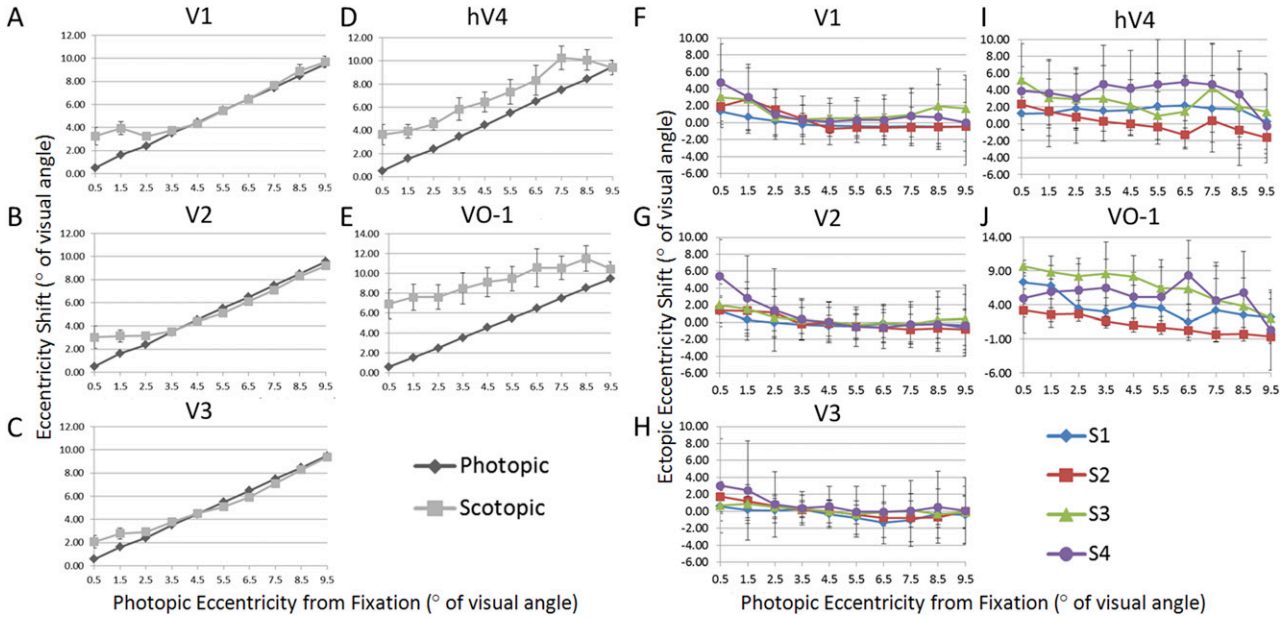

Fig. S6. Shifts in eccentricity representation across photopic and scotopic conditions. (*A*–*E*) Each graph displays eccentricity representation for photopic (dark gray lines with diamonds) and scotopic (light gray lines with squares) conditions in a single visual field map as a function of preferred eccentricity under photopic conditions averaged across subjects. (*A*) V1 pRF shifts. (*B*) V2 pRF shifts. (*C*) V3 pRF shifts. (*D*) hV4 pRF shifts. (*E*) VO-1 pRF shifts. Note that each map shows significant shifts outward from the rod scotoma in the central eccentricities. Error bars represent SEMs. (*F*–*J*) Each graph displays the ectopic eccentricity shift for each map for each individual subject. Positive numbers indicate shifts away from the scotoma (more eccentric from fixation). (*F*) V1 shift. (*G*) V2 shift. (*H*) V3 shift. (*I*) hV4 shift. (*J*) VO-1 shift. The legend indicates the color and marker shape for each subject. Error bars represent SDs.

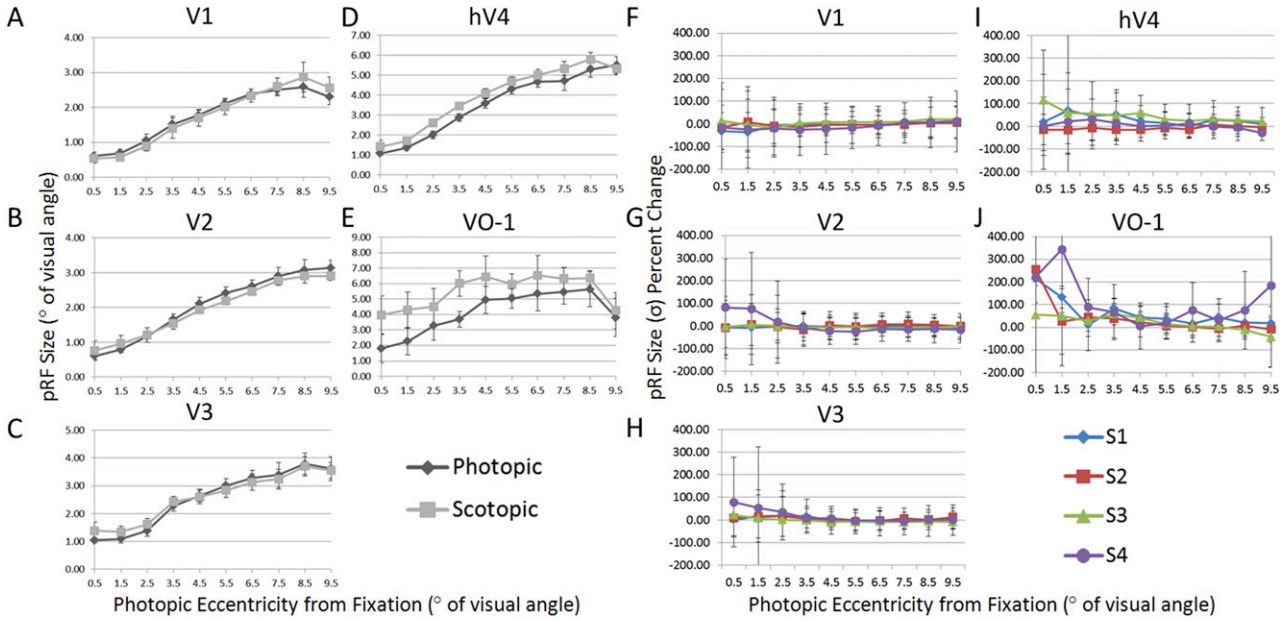

Fig. S7. pRF size (σ) measurements across photopic and scotopic conditions. (*A–E*) Each graph displays pRF size for photopic (dark gray lines with diamonds) and scotopic (light gray lines with squares) conditions in a single visual field map as a function of preferred eccentricity under photopic conditions averaged across subjects. (*A*) V1 pRF sizes. (*B*) V2 pRF sizes. (*C*) V3 pRF sizes. (*D*) hV4 pRF sizes. (*E*) VO-1 pRF sizes. Error bars represent SEMs. (*F–J*) Each graph displays the pRF size (σ) percentage change for each map for each individual subject. (*F*) V1 pRF size change. (*G*) V2 pRF size change. (*H*) V3 pRF size change. (*I*) hV4 pRF size change. (*J*) VO-1 pRF size change. The legend indicates the color and marker shape for each subject. Error bars represent SDs.

Table S1. Eye movement measurements

	Eyes ROI						Control V1 ROI					
	Photopic fixation		Scotopic fixation		Saccadic eye movements		Photopic fixation		Scotopic fixation		Saccadic eye movements	
Subject	Mean	SEM	Mean	SEM	Mean	SEM	Mean	SEM	Mean	SEM	Mean	SEM
S1	1.43	0.11	2.19	0.27	8.40	0.66	0.36	0.02	0.29	0.02	0.59	0.02
S3	2.20	0.16	1.38	0.30	5.98	0.25	0.27	0.03	0.30	0.02	1.04	0.06
S4	2.35	0.26	2.88	0.32	11.95	1.67	0.35	0.02	0.34	0.05	0.51	0.03
Average	1.99	0.12	2.15	0.20	8.78	0.68	0.33	0.02	0.31	0.02	0.71	0.03

Rows for S1–S3 represent measurements of BOLD modulation from individual subjects. Average represents their average. Means are average SDs across scans. Data from the Eyes ROI (Fig. S4*D*) and the V1 ROI (Fig. S4*H*) are shown. Saccadic eye movement scans were not available for subject 2 for comparison here. In general, the more that the subjects moved their eyes, the higher the variations in BOLD as measured by the mean SDs (means) for measurements from the Eyes ROI. A paired samples *t* test reveals that there is not a significant difference in average SDs between photopic and scotopic conditions in the Eyes ROI [$t(2) = -0.318$, $P = 0.781$], indicating no difference in eye movements. For comparison, the average SD in the Eyes ROI is significantly higher for an eye saccade task than scotopic conditions [$t(2) = -5.070$, $P = 0.037$]. A paired samples *t* test reveals no difference between photopic and scotopic conditions in the V1 ROI [$t(2) = 0.574$, $P = 0.624$] or scotopic and eye saccade conditions [$t(2) = -2.339$, $P = 0.144$], ruling out task differences unrelated to eye movements between the eye saccade and scotopic conditions in the Eyes ROI comparisons.

Table S2. Results of statistical analyses

	Central		Peripheral	
Map	*F*	*P*	*F*	*P*
Coherence difference				
V1	24.347	0.016	4.070	0.137
V2	11.327	0.044	6.951	0.078
V3	27.564	0.013	5.828	0.095
hV4	0.459	0.621	0.412	0.567
VO-1	0.698	0.465	0.020	0.897
Eccentricity shift				
V1	18.545	0.023	0.133	0.740
V2	10.315	0.049	4.295	0.130
V3	12.924	0.037	2.009	0.251
hV4	11.875	0.041	3.311	0.166
VO-1	15.389	0.029	6.040	0.091
pRF size change				
V1	8.417	0.062	0.289	0.628
V2	0.803	0.436	2.688	0.200
V3	4.247	0.131	2.168	0.237
hV4	2.147	0.239	0.915	0.409
VO-1	24.948	0.015	1.562	0.300

All *F* values and their associated *P* values reported are the results of multivariate ANOVAs with one hypothesis degree of freedom and three error degrees of freedom. Because one test was performed per hypothesis, no correction for multiple comparisons was necessary. Thus, the threshold for statistical significance was 0.05 in all cases. See *Results* for more details.